Journal of Materials Chemistry A



PAPER

View Article Online



Cite this: J. Mater. Chem. A, 2018, 6,

MOF-derived α -NiS nanorods on graphene as an electrode for high-energy-density supercapacitors†

Chong Qu,‡^{ab} Lei Zhang,‡^b Wei Meng,‡^a Zibin Liang,^a Bingjun Zhu,^a Dai Dang,^b Shuge Dai,^b Bote Zhao, ^b Hassina Tabassum,^a Song Gao,^a Hao Zhang,^a Wenhan Guo, a Ruo Zhao, a Xinyu Huang, a Meilin Liu b *b and Rugiang Zou b *a

Hierarchically porous electrodes made of electrochemically active materials and conductive additives may display synergistic effects originating from the interactions between the constituent phases, and this approach has been adopted for optimizing the performances of many electrode materials. Here we report our findings in design, fabrication, and characterization of a hierarchically porous hybrid electrode composed of α -NiS nanorods decorated on reduced graphene oxide (rGO) (denoted as R-NiS/rGO), derived from water-refluxed metal-organic frameworks/rGO (Ni-MOF-74/rGO) templates. Microanalyses reveal that the as-synthesized α -NiS nanorods have abundant (101) and (110) surfaces on the edges, which exhibit a strong affinity for OH- in KOH electrolyte, as confirmed by density functional theorybased calculations. The results suggest that the MOF-derived α-NiS nanorods with highly exposed active surfaces are favorable for fast redox reactions in a basic electrolyte. Besides, the presence of rGO in the hybrid electrode greatly enhances the electronic conductivity, providing efficient current collection for fast energy storage. Indeed, when tested in a supercapacitor with a three-electrode configuration in 2 M KOH electrolyte, the R-NiS/rGO hybrid electrode exhibits a capacity of 744 C g^{-1} at 1 A g^{-1} and 600 C g^{-1} at 50 A g^{-1} , indicating remarkable rate performance, while maintaining more than 89% of the initial capacity after 20 000 cycles. Moreover, when coupled with a nitrogen-doped graphene aerogel (C/NG-A) negative electrode, the hybrid supercapacitor (R-NiS/rGO/electrolyte/C/NG-A) achieved an ultra-high energy density of 93 W h kg⁻¹ at a power density of 962 W kg⁻¹, while still retaining an energy density of 54 W h kg⁻¹ at an elevated working power of 46 034 W kg⁻¹.

Received 20th December 2017 Accepted 24th January 2018

DOI: 10.1039/c7ta11100b

rsc.li/materials-a

Introduction 1

With the rapid advancements in emerging technologies (e.g. electric vehicles and smart grids) and the increasingly strong desire for a clean and sustainable energy future, the demand for highly efficient and more powerful energy storage systems and technologies has become an urgent challenge facing us today. Supercapacitors (SCs) are considered promising energy storage devices because of their high specific power density, fast charge-discharge rate, long cycle life, and pollution-free operation. 1-3 In particular, hybrid supercapacitors (HSCs) composed of a capacitive electrode (based on an electric double layer) and

^aBeijing Key Laboratory for Theory and Technology of Advanced Battery Materials,

a battery-type electrode (involving a fast redox reaction) have attracted great attention because they have the potential to achieve high energy density by broadening the operating voltage and increasing the capacitance of the hybrid devices.4-6 In a typical HSC, the negative electrode could be made of active carbon or graphene-based carbon materials,7-9 whereas the positive electrode could be based on an intercalation compound or a transition metal compound.7,9-18 Recently, advances have been made in enhancing the performance of capacitive electrodes in our group by successfully synthesizing a Co(mIM)2modified (mIM = 2-methylimidazole) nitrogen-doped graphene aerogel (C/NG-A), achieving a relatively high specific capacitance (ca. 400 F g^{-1} at 1 A g^{-1})¹⁵ and excellent rate capability while maintaining good cycling stability (99.7% capacitance retention after 20 000 cycles). Therefore, the development of advanced battery-type positive electrodes will be essential in an effort to make good use of the C/NG-A electrode in the development of a long cycle-life HSC with high energy and power

Metal-organic frameworks (MOFs) represent an important class of crystalline, nanoporous materials, which have been

Department of Materials Science and Engineering, College of Engineering, Peking University, Beijing 100871, P. R. China. E-mail: rzou@pku.edu.cn ^bSchool of Materials Science and Engineering, Georgia Institute of Technology, 771

Ferst Drive, Atlanta, GA 30332, USA. E-mail: meilin.liu@mse.gatech.edu

[†] Electronic supplementary information (ESI) available. See DOI: 10.1039/c7ta11100b

[‡] These authors share equal contribution to this work.

used for many applications because of their exceptional porosity, high specific surface area, controllable morphology, and multifunctionalities.19-22 For example, MOFs-as-template synthesis is considered one of the most promising strategies for the preparation of SC active materials as MOFs could be easily converted to battery-type materials or carbons with a much higher surface area and a diverse range of functionalities compared to conventionally synthesized materials. 23-26 Recently, MOF-74 materials ($M_2(DOBDC)$; M = metal, DOBDC 2,5-dihydroxy-1,4-benzenedicarboxylate), a subclass of MOFs demonstrating 1-dimensional (1-D) hexagonal pores lined with square-pyramidal open metal sites, have demonstrated high capacity when used as templates for the synthesis of porous carbons or battery-type metal-oxides or hydroxides.27-29 However, the rate capabilities and cycling stabilities of these pristine MOF-74-derived materials are comparatively poor. Specifically, one efficient solution is to integrate batterytype electrode materials with graphene, a 2-D "aromatic" monolayer carbon material.30-32 The advantages of a hybrid electrode architecture comprising graphene sheets and inorganic nanomaterials include (1) effective improvement of the electrical connectivity between the individual electroactive species and shortening of the path for ionic transport through the electrolyte path;³³ and (2) the intimate mixing of the two phases, allowing synergistic interactions between them,34 and improving the overall electrochemical thus greatly performance.

Herein, we report a hybrid electrode composed of active site-enriched NiS nano-rods and reduced graphite oxide (denoted as R-NiS/rGO), derived from a facile in situ sulfuration transformation from the parent hybrid Ni-MOF-74/ rGO architecture. Inspired by the work of Cadot et al.,35 we synthesized Ni-MOF-74/rGO from a one-pot reflux method in water (denoted as R-Ni-74/rGO) instead of the conventional solvothermal (water-DMF-ethanol solution) strategy.36 Specifically, uniformly dispersed NiS nanorods (ca. 200 × 800 nm) derived from the nanocrystallized MOF-74 were successfully wrapped by rGO; the presence of rGO provides the desirable electronic conductivity for fast energy storage and the hierarchically porous structure of the nanohybrid facilitates rapid access of the liquid electrolyte to active materials. Besides, the surfaces of the NiS nanorods in the R-NiS/rGO hybrid electrode are very active for fast redox reactions, as confirmed by experimental measurements and density functional theory (DFT)-based calculations. When tested in a three-electrode configuration, the hybrid electrode exhibited high specific capacity, excellent rate capability, and good cycling performance. Moreover, a hybrid device with the R-NiS/rGO as the positive electrode and C/NG-A as the negative electrode (denoted as R-NiS/rGO/ electrolyte/C/NG-A) was fabricated, delivering a greatly enhanced gravimetric energy density of 92 W h kg⁻¹ and superior cycling stability compared to those recently reported for asymmetric/hybrid SCs.7,27,30,33,37,38 Further, the MOF/rGO hybrid-as-template is an effective strategy for synthesizing battery-type electrode materials with unique properties for high performance SCs.

2 Experimental

2.1 Synthesis of graphene oxide (GO)

Graphite oxide (GO) was fabricated from graphite powder by a modified Hummers method. 39,40 Typically, 2.5 g of K2S2O8 and 2.5 g of P₂O₅ were dissolved in 12 mL of concentrated H₂SO₄ with 2.5 g of P₂O₅, and then heated to 80 °C, followed by adding 3 g of graphite powder. The mixture was kept at 80 °C for 4.5 h before cooled down to room temperature. Then, 500 mL of deionized (DI) water was added into the mixture. The diluted solution was kept overnight and then filtered and washed with DI water. The resulting product was dried in air overnight to obtain the preoxidized graphite powder. Afterwards, the powder was added into 120 mL of cold (0 °C) concentrated H₂SO₄, and 15 g of KMnO₄ was then added slowly under stirring during which the solution temperature was kept below 20 °C. The mixture was stirred at 35 °C for 2 h, followed by slow addition of 250 mL of DI water in an ice bath to keep the temperature below 50 °C. The resulting mixture was stirred for another 2 h, and then 700 mL of DI water was added, followed by injecting 20 mL of 30% H₂O₂ immediately into the mixture. The solution was kept for 12 h, and the supernatant was removed. The left solution was washed with 10% diluted HCl and 1 L of DI water. In the final step, the GO dispersion was purified by dialysis for 7 days. The final concentration of the GO dispersion was ca. 15 mg mL $^{-1}$.

2.2 Synthesis of Ni-MOF-74/GO

The synthesis of Ni-MOF-74/GO was based on a previous report with a little modification.30 In a 100 mL round-bottom flask equipped with a condenser, the ligand 2,5-dihydroxy-1,4benzenedicarboxylic acid (0.516 g, 2.6 mmol) was added to an aqueous suspension of graphene oxide (GO, 3.13 mg mL⁻¹, 24 mL). After ultrasonic treatment for 10 min, the mixture was heated to reflux under strong magnetic stirring (oil bath at 160 °C). In a separate flask, nickel acetate tetrahydrate (1.260 g, 5 mmol) was dissolved in deionized water (5 mL) at 80 °C. The as-obtained light green nickel salt solution was added to the boiling suspension in one portion under continuous stirring. The mixture was further heated under reflux for 2 h. After cooling down to room temperature, the suspension was left for precipitation of the product. Then the supernatant was decanted and deionized water was again introduced for exchange. This process was repeated 3 times (until the pH value of the supernatant was ca. 7). The final product was obtained by freeze-drying. Upon freezing, the loose layered structure of the composite was first immobilized through the formation of the ice crystals. Afterwards, the ice crystals sublimated during freeze drying.

2.3 Synthesis of pure Ni-MOF-74

The synthesis of pure Ni-MOF-74 was based on a previous report with some modification.³⁰ In a 250 mL round-bottom flask equipped with a condenser, a suspension of 2,5-dihydroxy-1,4-benzenedicarboxylic acid (5.16 g, 26 mmol) in deionized water (200 mL) was heated to reflux under strong magnetic stirring

(oil bath at 160 °C). In a separate flask, nickel acetate tetrahydrate (12.60 g, 50 mmol) was dissolved in deionized water (50 mL) at 80 °C. The light green nickel salt solution obtained was added to the boiling suspension in one portion under continuous stirring. After a few minutes, a yellow precipitate started to form. The reaction mixture was further refluxed for 2 h. The final suspension was centrifuged and the yellow powder was washed three times with 100 mL portions of warm deionized water before being dried overnight at 80 °C.

2.4 Synthesis of pure R-NiS/rGO

The as-synthesized Ni-MOF-74/rGO was uniformly mixed with sublimed sulfur with a mass ratio of 1:1 (30 mg for both samples). The mixture was then placed in a corundum crucible and transferred to a tube furnace. R-NiS/rGO was synthesized at 350 °C under 5% H₂S-95% argon gas flow with a ramp rate of 2 °C min⁻¹, and then kept at 350 °C for 2 h. The furnace was naturally cooled to room temperature in argon, and the black powder was taken out and stored for further use.

2.5 Synthesis of pure N-NiS

N-NiS was synthesized from a 30 mg Ni-MOF-74-30 mg sublimed sulfur mixture at 350 °C in a 5% H₂S-95% Ar atmosphere with a ramp rate of 2 °C min⁻¹, and then kept at 350 °C for 2 h. The furnace was naturally cooled to room temperature, and the black powder was taken out and stored for further use.

Synthesis of C/NG-A

The C/NG-A was synthesized based on a recent report. 15 Firstly, a nitrogen-doped graphene aerogel (NG-A) was fabricated by the following steps: 2.5 mL of GO dispersion was diluted with 8 mL of DI water, followed by sonication for 2 h before adding 10 mL of NH₄OH. The mixture was stirred for 1 h and then sealed in a Teflon-lined autoclave. The hydrothermal reaction was carried out at 160 °C for 24 h to get a cylinder-like hydrogel. The resulting hydrogel was immersed in DI water, which was exchanged with fresh DI water several times to completely remove the residual NH₄OH. Secondly, Co(mIM)₂modified NG-A was synthesized. Typically, 0.144 g of Co(NO₃)₂·6H₂O and 0.324 g of 2-methylimidazole were each dissolved in 10 mL of methanol. The suspension was poured into the latter ligand solution under vigorous stirring. After 60 s of stirring, NG-A was added into the mixture, and kept at room temperature for 24 h. Later, the cylinder-like gel was taken out and immersed into ethanol. The ethanol was exchanged with fresh ethanol several times in order to remove the residual reagent. Afterwards, the resulting sample was dried using supercritical carbon dioxide, leading to the Co(mIM)2-modified NG-A. C/NG-A was synthesized by pyrolyzing the Co(mIM)₂-modified NG-A at 750 °C in a temperature-programmed furnace under an argon gas flow for 2 h. The furnace was cooled down to room temperature naturally in an argon atmosphere. Then the pyrolyzed sample was treated with concentrated hydrochloric acid at 80 °C for 6 h. The resulting sample was collected by centrifugation, washed with DI water, and then dried at 80 °C.

Results and discussion 3

Characterization of the R-NiS/rGO nanohybrids

The schematic illustration of the detailed formation process of the R-NiS/rGO is depicted in Fig. 1. The Ni-MOF-74/rGO precursors were synthesized by mixing the Ni(II)-containing solution and GO suspension through refluxing in water, followed by freeze drying to maintain the morphology of rGO. The Ni-MOF-74/rGO was mixed with sulfur powder and further treated by a facile reaction in 5 wt% H2S at 350 °C in a sealed tube furnace to obtain the R-NiS/rGO. For SC performance comparison, neat Ni-MOF-74-derived NiS was also prepared by the same synthesis method. The product was denoted as N-NiS.

Field emission scanning electron microscopy (FE-SEM) was performed to investigate the microstructure and morphology of the as-synthesized samples. It is obvious to see that the sizes of the MOFs in the hybrid material were significantly reduced to the nanoscale (ca. 300 × 1200 nm) compared with pristine micron-sized MOF-74 in Fig. 1 and S1,† and the NiS remained to be a rod-like nanostructure after sulfuration with an even smaller average size of ca. 200×800 nm. The SEM images in Fig. S1b and d† show that the graphene sheets were successfully intertwined and intimately bounded by the uniformly dispersed MOF-74 and NiS nanorods. Besides, unlike the common drying method, freeze-drying effectively avoided the agglomeration of the graphene sheets and helped keep the loose layered architecture of the nanohybrids. Additionally, surface elemental distribution was acquired using energy dispersive spectroscopy (EDS) to elucidate the composition of R-NiS/rGO (Fig. S2, ESI†). By reading the survey spectrum, it is obvious to find that R-NiS/ rGO is composed of Ni, S, C, and O exclusively.

The crystallinities of the as-prepared Ni-MOF-74 and MOF-74/rGO were confirmed by comparing the powder X-ray diffraction (PXRD) pattern with the simulated one in Fig. S3 in the ESI.†36 From the enlarged MOF-74/rGO pattern (inset of Fig. S3, ESI†), the carbon (002) and (100) signals indicate the successful transformation from GO to rGO during refluxing. Fig. 2a shows the PXRD pattern of R-NiS/rGO and N-NiS. It is obvious to see that all the MOF characteristic peaks disappear, and apart from the carbon (002) signal, other peaks in both samples could be indexed to the (100), (101), (102), and (110) plane reflections of α-NiS (JCPDS: 02-1280) very well.41 The presence of graphene is also proved by Raman spectra depicted in Fig. 2b. The characteristic D and G bands for carbon materials are observed at 1330 and 1595 cm⁻¹. Compared with the N-NiS, the I_D/I_G value of the R-NiS/rGO increased obviously, which means that there are more defects in the NiS/rGO, indicating that graphene and NiS species are intimately hybridized in the hybrid structure. The porous features of R-NiS/rGO were examined by using nitrogen physisorption isotherms at 77 K as depicted in Fig. 2c. The adsorption-desorption isotherms are classified as IUPAC type IV with a type H2 hysteresis loop observed in the range of 0.5–1.0 P/P_0 , indicating the formation of mesopores in the architecture. Quenched solid state functional theory (QS-DFT) was applied to further assess the pore size distributions of R-NiS/rGO (inset of Fig. 2c). Compared with

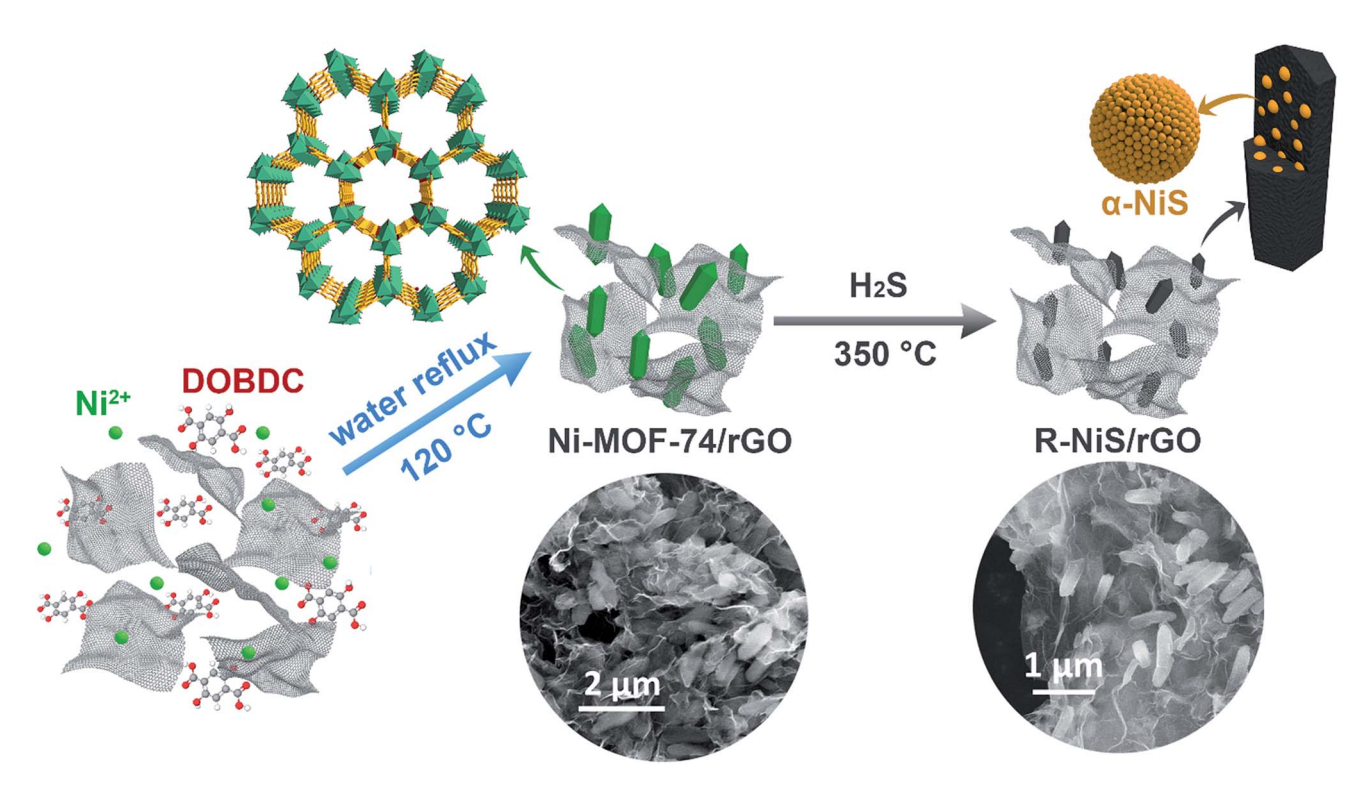


Fig. 1 Schematic illustration of the synthesis procedure of the R-NiS/rGO from MOF precursors.

the isotherms of Ni-MOF-74 and Ni-MOF-74/rGO (Fig. S4, ESI†), we can see that unlike the neat MOF-74 which only demonstrated micropores, R-NiS/rGO inherited the mesoporous feature from the parent Ni-MOF-74/rGO and exhibited hierarchical porous nature with an appealing distribution of 3-35 nm. These hierarchical pores will keep the contact areas between active materials and electrolyte large and sufficient during electrochemical charge-discharge processes, thus effectively reducing the self-aggregation of the hybrid structure.42 A transmission electron microscope (TEM) was applied to further analyze the morphology and structure of R-NiS/rGO nanohybrids. As shown in Fig. 2d and S5,† the rod-like NiS which is closely intertwined with graphene sheets is an aggregated structure formed by disorderly stacked NiS nanoparticles (ca. 8 nm), which is in good agreement with the SEM results. The High-Angle Annular Dark-Field Scanning Transmission Electron Microscopy (HADDF-STEM) images shown in Fig. 2e clearly reveal that Ni and S are homogeneously distributed on the nanorods, while C exists throughout the whole structure.

X-ray photoelectron spectroscopy (XPS) measurements were performed to analyze the surface electronic state and composition of R-NiS/rGO. The presence of elements C, O, Ni, and S has been supported by the survey scan spectrum (Fig. S6, ESI†), which is consistent with the EDS results. For the C 1s XPS spectrum of the nanohybrid, signals including the aromatic-linked carbon (C=C, 284.6 eV), the C in oxygen single-bonded carbon bonds (C=O, 285.2 eV), the carbonyl carbon (C=O, 286.4 eV), and the carboxylate carbon (O-C=O, 288.9 eV) can be observed (Fig. 2f), indicating that there are oxygen-containing functional groups on the graphene sheets. ²⁶ These functional

groups are highly active for anchoring Ni–S species during the synthesis process, thus greatly enhancing the structural stability of the nanohybrids. Fig. 2g shows the high-resolution spectrum of Ni 2p. The observed Ni $2p_{1/2}$ and Ni $2p_{2/3}$ peaks centered at 873.7 and 856.1 eV (with a 17.6 eV difference), along with two corresponding satellites, are consistent with those of NiS. The S 2p spectrum in Fig. 2h can also be divided and fitted to the strong peaks at 163.2 eV $(2p_{3/2})$ and 162.0 eV $(2p_{1/2})$, which correspond to the Ni–S bonds and the S²⁻ in low coordination on the surface, respectively. Respectively.

3.2 Electrochemical performance of the R-NiS/rGO nanohybrids

To evaluate the electrochemical performance, the assynthesized samples were tested in a three-electrode configuration in 2 M KOH aqueous solution. The cyclic voltammograms (CVs) of the R-NiS/rGO and N-NiS at a constant scan rate of 10 mV s⁻¹ are depicted in Fig. 3a. Both curves have a similar shape with a pair of well-defined redox peaks at 0.2 and 0.35 V, indicating that the capacity is attributed to the two-phase Ni²⁺/ Ni³⁺ faradaic reaction. Besides, it is clear to see that the R-NiS/ rGO exhibits a higher current density and larger integral area than N-NiS, implying a significantly improved specific capacity and fast redox reaction kinetics process of the R-NiS/rGO sample. With increasing scan rates from 10 to 100 mV s^{-1} the corresponding currents in Fig. 3b show a rising trend accordingly, indicating the good rate capability of the active material. The galvanostatic charge-discharge (GCD) tests are carried out at different current densities (1 to 50 A g⁻¹). As

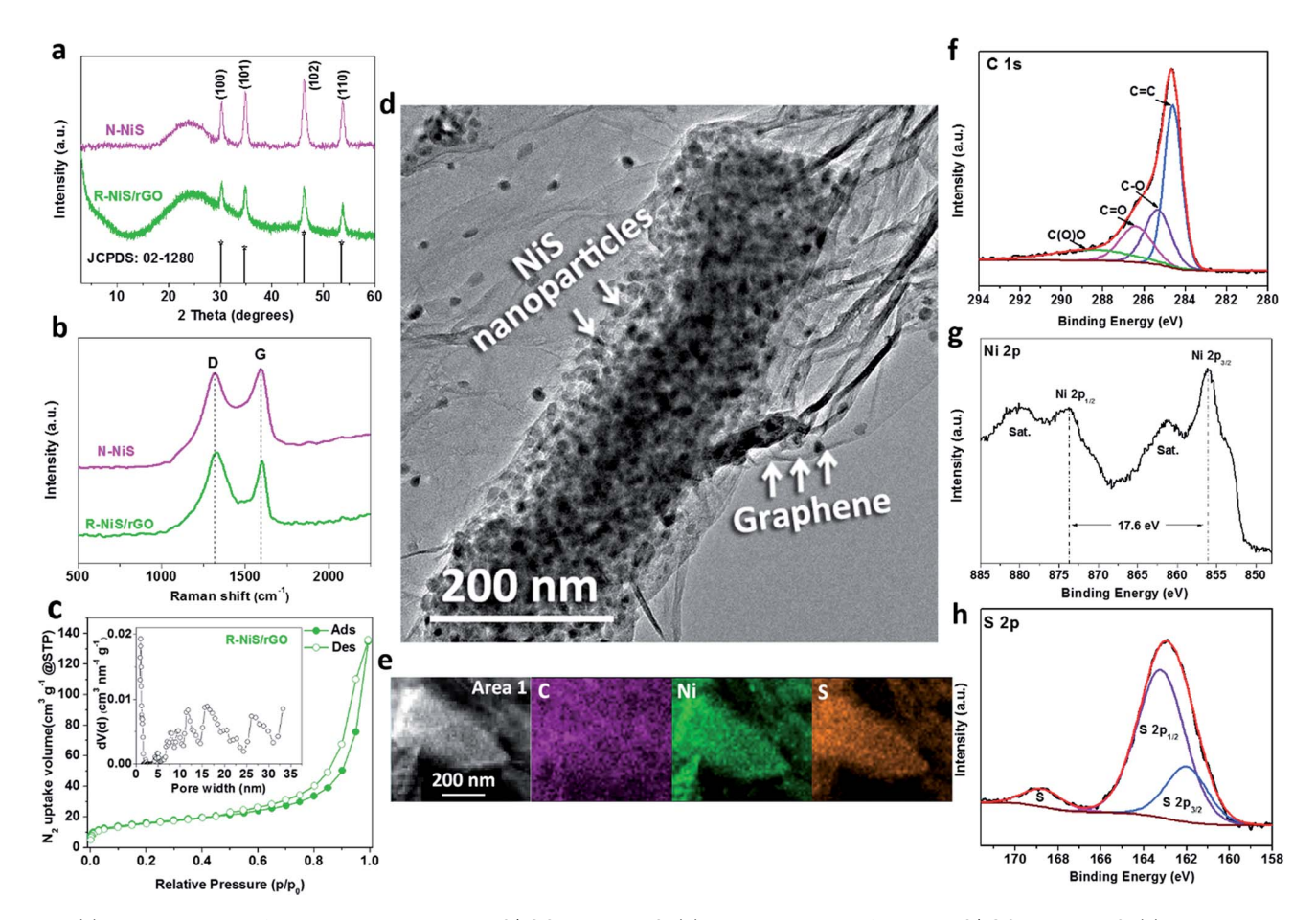


Fig. 2 (a) PXRD patterns of the as-synthesized R-NiS/rGO and N-NiS. (b) Raman spectra of the R-NiS/rGO and N-NiS. (c) N2 adsorptiondesorption isotherms and the corresponding pore size distribution plot (inset) of R-NiS/rGO. (d) TEM image of the R-NiS/rGO. (e) HAADF-STEM image and the corresponding EDS elemental mappings of C, Ni, and S. (f and h) High resolution XPS spectra of C 1s, Ni 2p, and S 2p of the R-NiS/ rGO.

shown in Fig. 3c, there are plateaus between 0.25 and 0.35 V with a relatively small slope prevailing over a wide capacity range, and all the curves exhibit a high coulombic efficiency due to the highly reversible redox reactions of the R-NiS/rGO nanohybrids. For comparison, the CV and GCD curves of the N-NiS sample are depicted in Fig. S7 (ESI†).

The specific capacities of the as-obtained R-NiS/rGO and N-NiS were calculated from the GCD curves at all current densities, and the calculation was based on the entire mass of both components (Fig. 3d). R-NiS/rGO exhibits a capacity of 744 C g⁻¹ at 1 A g⁻¹ and can achieve as high as 600 C g⁻¹ at an elevated current density of 50 A $\rm g^{-1}$ with a capacity retention of 80%. In contrast, in the case of the N-NiS, the slope shows a sharp decrease of capacity to 260 C g^{-1} at 20 A g^{-1} which is 52% of the initial value. The cycling stabilities of the aforementioned samples were further investigated at a current density of 20 A g^{-1} (Fig. 3f). The R-NiS/rGO electrode demonstrated a very attractive capacity retention of 89% even after 20 000 cycles, indicating a greatly improved cycling performance compared to the N-NiS (ca. 72%, 10 000 cycles). The greatly enhanced rate performance and cycling stability clearly show the good electronic conductivity of R-NiS/rGO, especially when applied at

high current densities, demonstrating that the NiS is intimately bounded by rGO in the hybrid. The promotion of electronic conductivity is further supported by the electrochemical impedance spectroscopy (EIS) tests. As shown in the Nyquist plots in 2 M KOH within the frequency ranges from 100 kHz to 10 MHz (Fig. 3e), it is obvious that R-NiS/rGO exhibited higher conductivity compared with N-NiS which exhibited a chargetransfer impedance of ca. 1.41 Ω . Specifically, a semicircle at high frequencies with a diameter of ca. 0.65 Ω along the real axis denotes the charge-transfer impedance at the electrode-electrolyte interface of the R-NiS/rGO electrode. This low charge transfer resistance is due to the intimate contact with conductive rGO and the good intrinsic electronic properties of metal sulfides. The low equivalent series resistance in a highfrequency region signifies the excellent conducting properties in aqueous electrolytes. Besides, the exposure of numerous active sites within the nanohybrids, and the shortened transport distance in the hierarchical nano-scaled structure also synergistically contribute to the enhanced SC performance to some degree. These remarkable electrochemical performances are highly comparable to those of battery-type electrode materials reported in the literature.

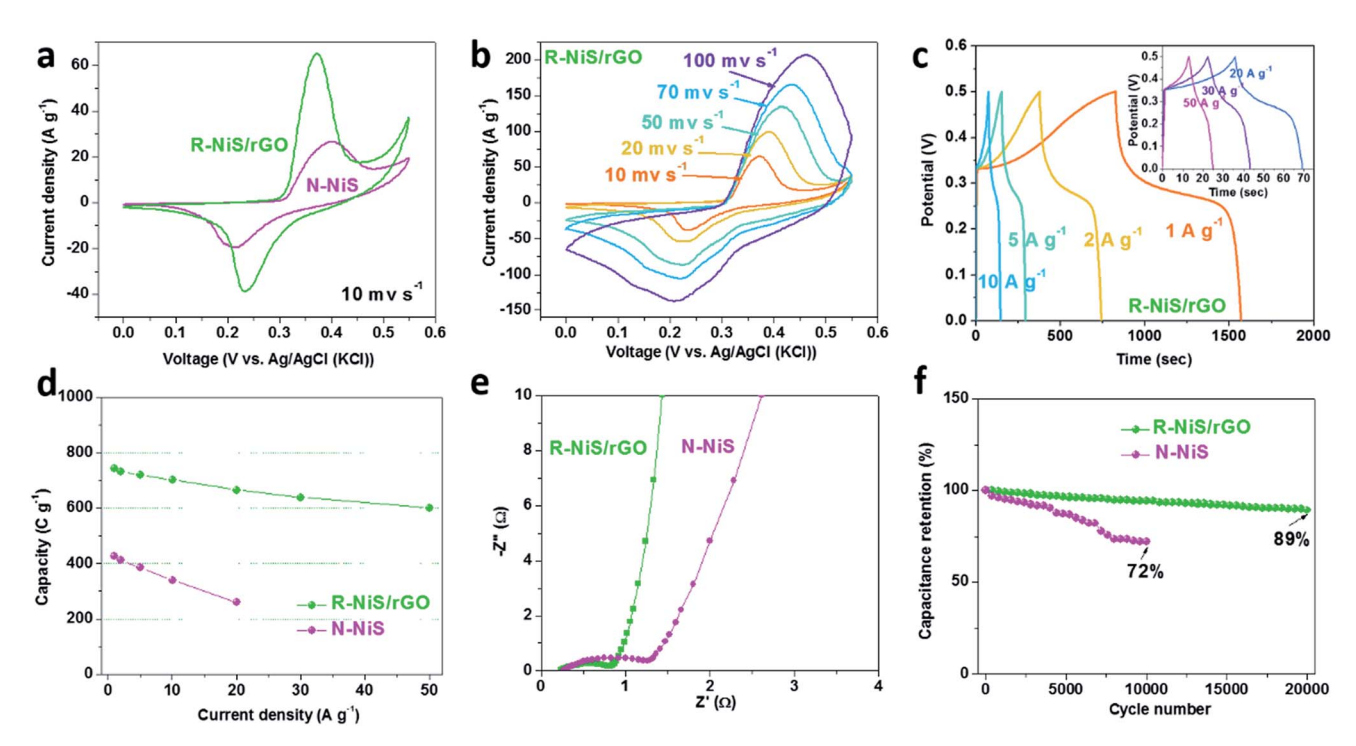


Fig. 3 Electrochemical properties: (a) CV curve comparison of R-NiS/rGO and N-NiS at 10 mV s $^{-1}$, (b) CV curves of R-NiS/rGO at various scan rates, (c) GCD curves of R-NiS/rGO at different current densities, (d) specific capacities of R-NiS/rGO based on different current densities, (e) Nyquist plots of R-NiS/rGO and N-NiS, and (f) cycling performances of R-NiS/rGO and N-NiS.

To further broaden the voltage window and enhance the energy density of the MOF-derived R-NiS/rGO for practical application. We constructed a hybrid SC by employing the R-NiS/rGO as the positive electrode and the as-reported capacitive Co(mIM)2-modified nitrogen-doped graphene aerogel (C/NG-A) as the negative electrode, as schematically illustrated in Fig. 4a. The morphology characterization and electrochemical tests of the C/NG-A are included in Fig. S8 (ESI†). Clearly, the C/NG-A exhibited an overall capacitive behavior with electrical double-layer contribution from both MOF-derived carbon and NG-A and slight pseudocapacitive contribution from the N doping on both the mIM ligand and NG-A between -1 and 0 V. Based on eqn S2 and S3 (ESI†), the charge balance was achieved by adjusting the mass ratio (R) between the negative electrode and the positive electrode to 2.2 (Fig. S9a, ESI†). The CV curves of the as-fabricated device are presented in Fig. 4b, an operating voltage of 1.6 V could be achieved, and the shapes of the curves were well maintained by increasing the scan rate from 10 mV s⁻¹ to 100 mV s⁻¹, suggesting the high rate capability of the hybrid device. GCD performances from 1 A g⁻¹ to 50 A g⁻¹ of the hybrid device are depicted in Fig. 4c, the curves are battery-type with a sloping plateau at all current densities and the symmetric shapes indicate high coulombic efficiencies. The specific capacitances calculated based on the total mass of both electrodes from the GCD curves corresponding rate performance are shown in Fig. S9b (ESI†), it is notable that more than 58% of the initial capacitance at 1 A g⁻¹ was retained even at an elevated current density of 50 A g^{-1} .

The Ragone plot, which demonstrates the relationship between energy densities and power densities of different devices, is shown in Fig. 4d. It can be seen that an energy density of 93 W h kg⁻¹ was achieved at the power density of 962 W kg⁻¹ for the R-NiS/rGO//C/NG-A hybrid device. Moreover, an energy density of 54 W h kg⁻¹ can be kept at an elevated working power of 46 034 W kg⁻¹. The gravimetric energy and power densities of the hybrid device are superior to those of other recently reported hybrid/asymmetric devices, including triple phase Ni_xS_y/rGO//G,³⁰ NiCo₂S₄//G,³⁷ NiCo₂S₄/N-carbon foam//ordered mesoporous C/N-carbon foam,38 MOF-74 derived 65Ni-35Co hydroxide//N-doped carbon,27 Ni-Co-Fe hydroxide//active carbon,7 and $Co_rNi_v(OH)_2(arGO//p$ phenylenediamine-modified rGO.33 Stability is another important property for the SCs, Fig. 4e demonstrates the cycling performance of the hybrid device between 0 and 1.6 V at 20 A g⁻¹. It is noted that the R-NiS/rGO//C/NG-A hybrid device displays a 93% capacitance retention of the initial value even after 10 000 cycles, indicating superb cycling stability.

3.3 Investigation of the high supercapacitor performance of R-NiS/rGO nanohybrids

The high resolution transmission electron microscopy (HR-TEM) image depicted in Fig. 5a reveals that MOF-derived NiS nanorods feature a rough surface and abundant edge sites with an average thickness of *ca.* 20 nm. To illustrate the difference between the edge and interior sites in NiS nanorods, areas marked with yellow (edge site) and blue (interior site) are randomly picked for further magnification. Fig. 5b shows the

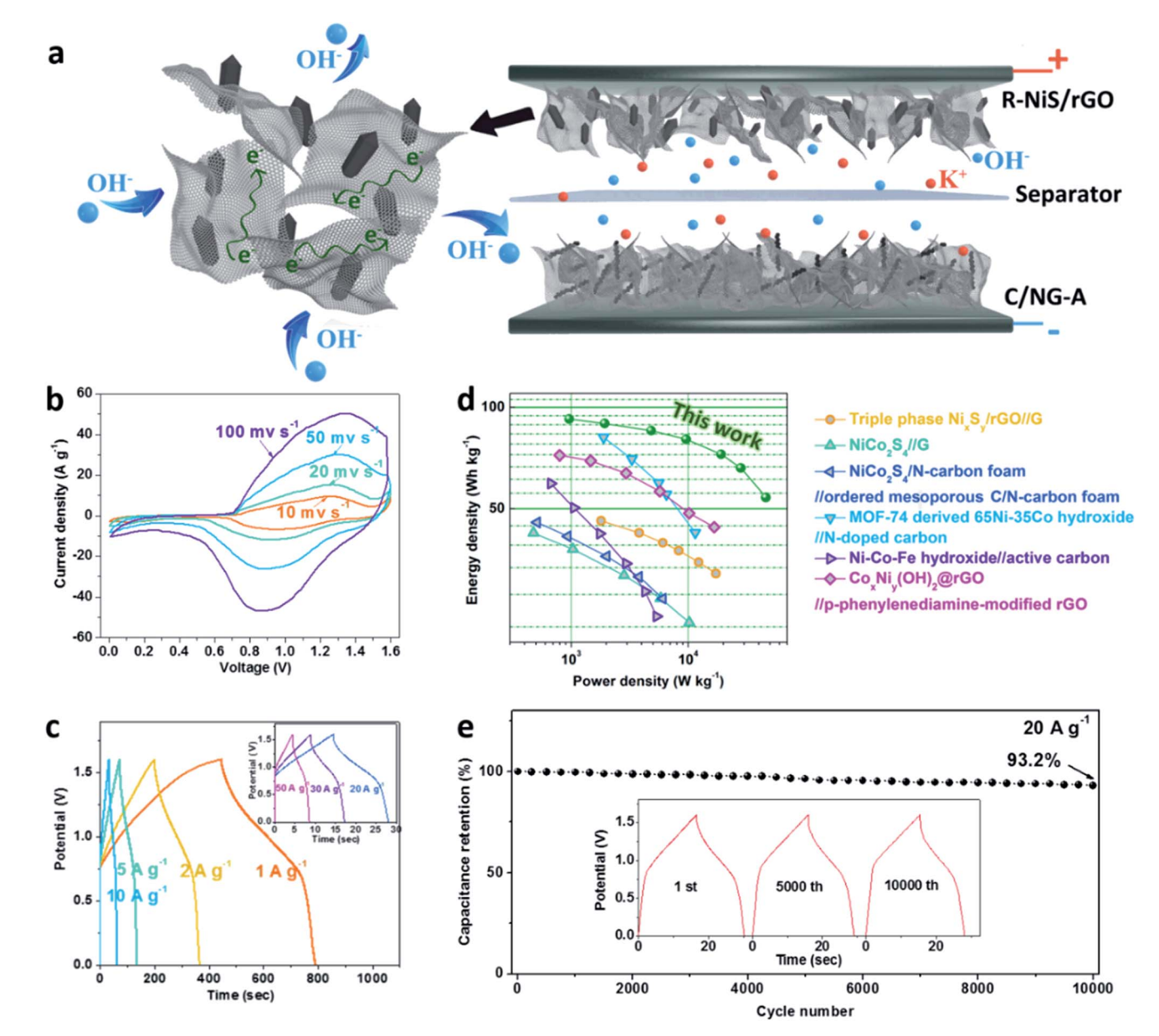


Fig. 4 Electrochemical performance of the two-electrode hybrid device: (a) schematic illustration of the hybrid device, (b) CV curves of the R-NiS/rGO//C/NG-A at various scan rates, (c) GCD curves of R-NiS/rGO//C/NG-A at different current densities, (d) Ragone plot of R-NiS/rGO//C/ NG-A, other recently reported high performance hybrid/asymmetric SCs are also listed for comparison, and (e) cycling stability of the R-NiS/ rGO//C/NG-A at a current density of 20 A g⁻¹ between 0 and 1.6 V, the inset in (e) shows the GCD curves at the 1st, 5000th, and 10 000th cycles.

enlarged image of the yellow area; the red regions are NiS nanoparticles anchored on the MOF-derived carbon sphere, in which only lattice fringes of 0.195 and 0.293 nm can be observed, ascribed to the (101) and (110) planes of α -NiS, respectively (Fig. 5d). However, from Fig. 5c and e which are the magnified images of the interior blue area, (102) planes with visible lattice fringes of 0.255 nm are obviously dominant compared with the yellow area, indicating (101) and (110) planes as preferential orientations for the edge sites of R-NiS/ rGO nanohybrids. This result is very interesting as edge sites always feature relatively good exposure to the electrolyte, and if (101) and (110) planes had better electrochemical activity

compared with the (102) plane, R-NiS/rGO will have a great chance to be a good electrochemical energy storage material.

To further understand the surface adsorption properties of α-NiS regarding OH⁻, first-principles calculations on (110), (102) and (101) planes were carried out. The slab structures are shown in Fig. S10.† The (110) plane is a 4-layer non-polar plane, with surface Ni and S coordination numbers as 4 and 4. The (102) plane is a 5-layer non-polar plane, with surface Ni and S coordination numbers as 4/5 and 4/5 (4/5 represents half 4 and half 5-coordination). The (101) plane is a 5-layer polar plane, with surface Ni and S coordination numbers as 4 and 2. Due to surface relaxation, the Ni-S plane in the (110) surface is

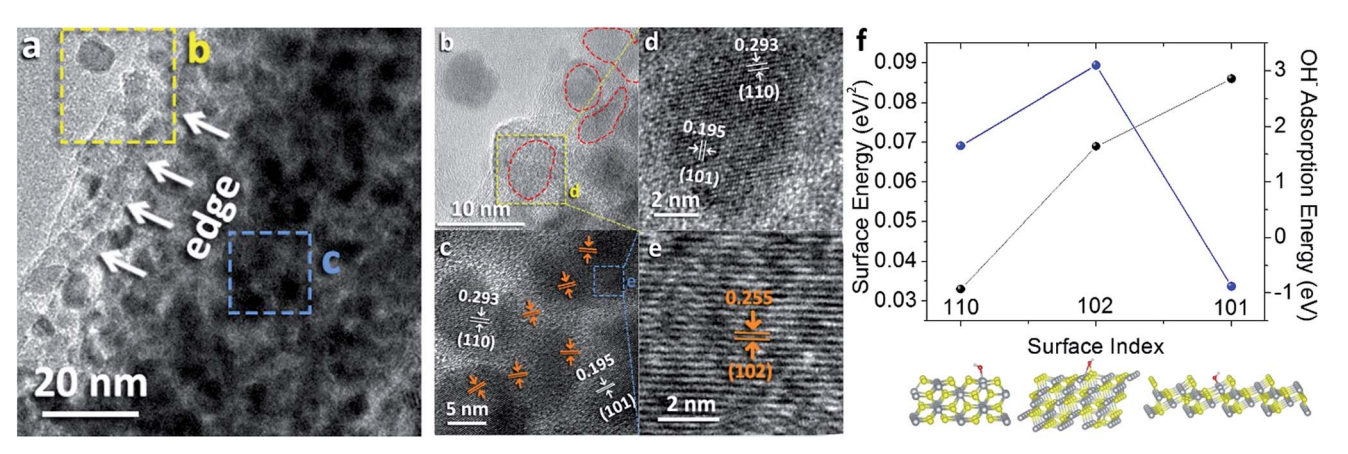


Fig. 5 (a) HR-TEM images of the R-NiS/rGO hybrid nanostructure. (b) and (c) Enlarged HR-TEM images from the yellow and blue squares in (a), respectively. (d) and (e) The visible lattice fringe images obtained from the yellow square in (b) and blue square in (c), respectively. (f) Surface energy and OH^- adsorption energy of different slabs of α -NiS from DFT calculations.

ruptured from planar. This occurs in (102) and (101) surfaces as well.

Based on eqn S7 (ESI \dagger), the calculated surface energies for (110), (102) and (101) slabs are 0.033, 0.069, and 0.086 eV Å $^{-2}$ (0.528, 1.098 and 1.371 J m $^{-2}$) which are depicted in Fig. 5f, respectively. This indicates that in thermodynamic equilibrium, if there is no solvent adsorption effect on these surfaces, (101) will be the most stable and enriched plane to be observed, followed by (102) and (110).

The OH⁻ adsorption energy that dictates the redox reaction charge-discharge kinetics was also calculated as the energy difference between OH⁻ after and before adsorption on surface Ni sites. The computed adsorption energies of OH⁻ for (110), (102) and (101) slabs from eqn S8 (ESI†) are 1.648, 3.101, and -0.879 eV (Fig. 5f), respectively. For the (102) plane, 4 and 5coordinated Ni has nearly degenerate adsorption energy. This is consistent with the relation that the higher surface energy plane has stronger adsorption behaviour in general, although (102) has an exceptionally positive adsorption energy. The adsorption behaviour is believed to be dictated by the coordination environment of surface Ni. Although the adsorption sites of surface Ni are all coordinated by 4 S atoms, the Ni-S bond lengths are very different. The (101) surface has the Ni-S bond with an average length of 2.15 Å, and (110) and (102) have the values of 2.23 and 2.35 Å. It is found that a longer (or weaker) Ni-S bond also indicates a weaker Ni-O bond. (101), (110) and (102) have Ni-O bond lengths as 1.83, 1.86 and 2.95 Å. It is very likely that hydroxide has negligible adsorption on the (102) surface due to the over 3 eV adsorption energy and large Ni-O bond length (even larger than S-O bond length 1.73 Å that is unlikely to form due to coulombic repulsion). On the other hand, the favorable adsorption of hydroxide species on the (101) surface is probably due to the unique surface kink naturally formed from surface cleavage that causes steric repulsion between hydroxide and surface atoms to go to minimum. It is thus energetically favorable for the (101) surface to do charge-discharge, followed by (110) and (102) surfaces on which a large over-potential is necessary to drive the electro-chemical process. Combined with

the TEM results which demonstrate dominant (101) and (110) surfaces on the edge of the NiS nanorod, the R-NiS/rGO nanohybrid is favorable for efficient transport of the electrolyte, thus improving the effective utilization of the active materials in the application of SCs.

4 Conclusions

In summary, we have successfully synthesized a hierarchically porous hybrid electrode composed of R-NiS and rGO by direct sulfuration of a MOF-74/rGO hybrid material (prepared by refluxing instead of a conventional hydrothermal reaction). When tested in a supercapacitor, the R-NiS/rGO hybrid electrode displayed high specific capacity, superb rate capability, and excellent cycle life, far better than those of other nickel sulfide-based electrodes ever reported. The enhanced electrochemical performance is attributed mainly to the (101) and (110) active site-enriched edges of the R-NiS/rGO hybrid, which exhibit a strong affinity for OH in 2 M KOH electrolyte, as confirmed by experimental measurements and DFT-based calculations. Furthermore and in particular, when coupled with a capacitive electrode C/NG-A to construct a hybrid supercapacitor with a configuration of R-NiS/rGO/electrolyte/C/ NG-A, the hybrid device showed very high energy densities and power densities. The developed methodology for the fabrication of hierarchically porous hybrid electrodes is applicable to the fabrication of other high-performance electrodes for various energy storage and conversion devices.

5 Author contributions

C. Q., R. Q. Z. and M. L. L. conceived the project. C. Q. prepared the electrodes, performed the electrochemical experiments, and analyzed data. L. Z. carried out the theoretical calculation. W. M. prepared the MOF hybrids. Z. B. L. carried out SEM and XRD measurements. B. J. Z. collected the XPS and Raman data. H. T., S. G. and H. Z. contributed to the synthesis of GO and TEM measurements. W. H. G., R. Z., and X. Y. H.

collected and analyzed the N2 adsorption-desorption data. D. D., S. G. D., and B. T. Z. assisted C. Q. with the electrochemical experiments. C. Q., Z. B. L., M. L. L., and R. Q. Z. contributed to the discussion of the results. C. Q. drafted the manuscript, and all authors contributed to the final version of the manuscript.

Conflicts of interest

Paper

There are no conflicts to declare.

Acknowledgements

This work was supported by the National Key Research and Development Program of China (2017YFA0206701), the National Program for Support of Top-notch Young Professionals, the Changjiang Scholar Program, the US National Science Foundation under award number DMR-1742828 and the Guangdong Innovative and Entrepreneurial Research Team Program (No. 2014ZT05N200). This work used the Extreme Science and Engineering Discovery Environment (XSEDE), which is supported by the National Science Foundation grant number TG-DMR140083.

References

- 1 V. Augustyn, J. Come, M. A. Lowe, J. W. Kim, P.-L. Taberna, S. H. Tolbert, H. D. Abruña, P. Simon and B. Dunn, Nat. Mater., 2013, 12, 518-522.
- 2 J. Chmiola, C. Largeot, P.-L. Taberna, P. Simon and Y. Gogotsi, Science, 2010, 328, 480-483.
- 3 P. Simon and Y. Gogotsi, Nat. Mater., 2008, 7, 845-854.
- 4 Y. Gogotsi, ACS Nano, 2014, 8, 5369-5371.
- 5 W. Wei, Z. Wang, Z. Liu, Y. Liu, L. He, D. Chen, A. Umar, L. Guo and J. Li, J. Power Sources, 2013, 238, 376-387.
- 6 S. Ci, Z. Wen, Y. Qian, S. Mao, S. Cui and J. Chen, Sci. Rep., 2015, 5, 11919.
- 7 H. Li, Y. Gao, C. Wang and G. Yang, Adv. Energy Mater., 2015, 5, 1401814.
- 8 S. Y. Kim, H. M. Jeong, J. H. Kwon, I. W. Ock, W. H. Suh, G. D. Stucky and J. K. Kang, Energy Environ. Sci., 2015, 8, 188-194.
- 9 J. Yan, Z. Fan, W. Sun, G. Ning, T. Wei, Q. Zhang, R. Zhang, L. Zhi and F. Wei, Adv. Funct. Mater., 2012, 22, 2632-2641.
- 10 M. Xie, S. Duan, Y. Shen, K. Fang, Y. Wang, M. Lin and X. Guo, ACS Energy Lett., 2016, 1, 814-819.
- 11 Y. Ma, H. Chang, M. Zhang and Y. Chen, Adv. Mater., 2015, 27, 5296-5308.
- 12 K. L. Knoche, D. P. Hickey, R. D. Milton, C. L. Curchoe and S. D. Minteer, ACS Energy Lett., 2016, 1, 380-385.
- 13 Q. Zhang, B. Zhao, J. Wang, C. Qu, H. Sun, K. Zhang and M. Liu, Nano Energy, 2016, 28, 475-485.
- 14 B. Zhao, R. Ran, M. Liu and Z. Shao, Mater. Sci. Eng., R, 2015, 98, 1-71.
- 15 W. Xia, C. Qu, Z. Liang, B. Zhao, S. Dai, B. Qiu, Y. Jiao, Q. Zhang, X. Huang and W. Guo, Nano Lett., 2017, 17, 2788-2795.

- 16 D. Xiong, X. Li, Z. Bai, J. Li, H. Shan, L. Fan, C. Long, D. Li and X. Lu, Electrochim. Acta, 2018, 259, 338-347.
- 17 L. Fan, X. Li, X. Song, N. Hu, D. Xiong, A. Koo and X. Sun, ACS Appl. Mater. Interfaces, 2018, 10, 2637-2648.
- 18 D. Xiong, X. Li, Z. Bai, J. Li, Y. Han and D. Li, Chem.-Eur. J., 2017, 23, 1-6.
- 19 R. Bendi, V. Kumar, V. Bhavanasi, K. Parida and P. S. Lee, Adv. Energy Mater., 2016, 6, 1501833.
- 20 R. R. Salunkhe, J. Tang, Y. Kamachi, T. Nakato, J. H. Kim and Y. Yamauchi, ACS Nano, 2015, 9, 6288-6296.
- 21 C. Qu, Y. Jiao, B. Zhao, D. Chen, R. Zou, K. S. Walton and M. Liu, Nano Energy, 2016, 26, 66-73.
- 22 Q. Wang, R. Zou, W. Xia, J. Ma, B. Qiu, A. Mahmood, R. Zhao, Y. Yang, D. Xia and Q. Xu, Small, 2015, 11, 2511-2517.
- 23 L. Wang, Y. Han, X. Feng, J. Zhou, P. Qi and B. Wang, Coord. Chem. Rev., 2016, 307, 361-381.
- 24 W. Meng, W. Chen, L. Zhao, Y. Huang, M. Zhu, Y. Huang, Y. Fu, F. Geng, J. Yu and X. Chen, Nano Energy, 2014, 8, 133-140.
- 25 R. R. Salunkhe, Y. V. Kaneti, J. Kim, J. H. Kim and Y. Yamauchi, Acc. Chem. Res., 2016, 49, 2796-2806.
- 26 L. Wang, T. Wei, L. Sheng, L. Jiang, X. Wu, Q. Zhou, B. Yuan, J. Yue, Z. Liu and Z. Fan, Nano Energy, 2016, 30, 84-92.
- 27 C. Qu, B. Zhao, Y. Jiao, D. Chen, S. Dai, B. M. deglee, Y. Chen, K. S. Walton, R. Zou and M. Liu, ACS Energy Lett., 2017, 2, 1263-1269.
- 28 P. Pachfule, D. Shinde, M. Majumder and Q. Xu, Nat. Chem., 2016, 8, 718-724.
- 29 S. Chen, M. Xue, Y. Li, Y. Pan, L. Zhu and S. Qiu, J. Mater. Chem. A, 2015, 3, 20145-20152.
- 30 S. Dai, B. Zhao, C. Qu, D. Chen, D. Dang, B. Song, J. Fu, C. Hu, C.-P. Wong and M. Liu, Nano Energy, 2017, 33, 522-
- 31 J. Yang, C. Yu, X. Fan, S. Liang, S. Li, H. Huang, Z. Ling, C. Hao and J. Qiu, *Energy Environ. Sci.*, 2016, **9**, 1299–1307.
- 32 Y. Hu, C. Guan, Q. Ke, Z. F. Yow, C. Cheng and J. Wang, Chem. Mater., 2016, 28, 7296-7303.
- 33 B. Zhao, D. Chen, X. Xiong, B. Song, R. Hu, Q. Zhang, B. H. Rainwater, G. H. Waller, D. Zhen and Y. Ding, Energy Storage Mater., 2017, 7, 32-39.
- 34 S. Li, D. Wu, C. Cheng, J. Wang, F. Zhang, Y. Su and X. Feng, Angew. Chem., Int. Ed., 2013, 52, 12105-12109.
- 35 S. Cadot, L. Veyre, D. Luneau, D. Farrusseng and E. A. Quadrelli, J. Mater. Chem. A, 2014, 2, 17757-17763.
- 36 T. G. Glover, G. W. Peterson, B. J. Schindler, D. Britt and O. Yaghi, Chem. Eng. Sci., 2011, 66, 163-170.
- 37 L. Shen, L. Yu, H. B. Wu, X.-Y. Yu and X. Zhang, Nat. Commun., 2015, 6, 6694.
- 38 L. Shen, J. Wang, G. Xu, H. Li, H. Dou and X. Zhang, Adv. Energy Mater., 2015, 5, 1400977.
- 39 N. I. Kovtyukhova, P. J. Ollivier, B. R. Martin, T. E. Mallouk, S. A. Chizhik, E. V. Buzaneva and A. D. Gorchinskiy, Chem. Mater., 1999, 11, 771-778.
- 40 W. S. Hummers Jr and R. E. Offeman, J. Am. Chem. Soc, 1958,
- 41 J. Yang, X. Duan, W. Guo, D. Li, H. Zhang and W. Zheng, Nano Energy, 2014, 5, 74-81.

- 42 L.-Q. Mai, F. Yang, Y.-L. Zhao, X. Xu, L. Xu and Y.-Z. Luo, *Nat. Commun.*, 2011, 2, 381.
- 43 J. Chen, K. Sheng, P. Luo, C. Li and G. Shi, *Adv. Mater.*, 2012, **24**, 4569–4573.
- 44 P. Chen, T. Y. Xiao, Y. H. Qian, S. S. Li and S. H. Yu, *Adv. Mater.*, 2013, **25**, 3192–3196.
- 45 S. Chen and S.-Z. Qiao, ACS Nano, 2013, 7, 10190-10196.
- 46 Y. Zhang, L. Zuo, L. Zhang, J. Yan, H. Lu, W. Fan and T. Liu, *Nano Res.*, 2016, **9**, 2747–2759.
- 47 W. Wei, L. Mi, Y. Gao, Z. Zheng, W. Chen and X. Guan, *Chem. Mater.*, 2014, **26**, 3418–3426.
- 48 W. Hu, R. Chen, W. Xie, L. Zou, N. Qin and D. Bao, *ACS Appl. Mater. Interfaces*, 2014, **6**, 19318–19326.